Next Materials 5 (2024) 100252

Contents lists available at ScienceDirect

Next Materials

journal homepage: www.sciencedirect.com/journal/next-materials

Research article

Self-organized topological insulator heterostructures via eutectic solidification of Bi_2Te_3-Te

Kingshuk Bandopadhyay [a,*], Marta Buza [b], Cheng Chen [c,1], Andrzej Materna [a], Kamil Szlachetko [b], Piotr Piotrowski [a,d], Hańcza B. Surma [a], Jolanta Borysiuk [e], Ryszard Diduszko [b], Alexei Barinov [f], Yulin L. Chen [c], Maria Kaminska [e], Dorota A. Pawlak [a,b,d,**]

[a] ENSEMBLE3 Centre of Excellence, Wolczynska 133, Warsaw 01-919, Poland
[b] Łukasiewicz Research Network – Institute of Microelectronics and Photonics, Wolczynska 133, Warsaw 01-919, Poland
[c] Department of Physics, Clarendon Laboratory, University of Oxford, Oxford OX1 3PU, UK
[d] Faculty of Chemistry, University of Warsaw, Pasteura 1, Warsaw 02-093, Poland
[e] Faculty of Physics, University of Warsaw, Pasteura 5, Warsaw 02-093, Poland
[f] Elettra-Sincrotrone Trieste, Trieste, Basovizza 34149, Italy

ARTICLE INFO

Keywords:
Topological insulators
Heterostructures
Eutectics
Self-organization
Bi_2Te_3
Micro-pulling down method

ABSTRACT

Topological insulators (TI) are generating increasing interest as a new state of matter and due to the potential use of topologically- protected gapless surface states in spintronic devices and quantum computing. However, challenges such as high sensitivity to the atmosphere, the low surface-to-volume ratio, and the need for various material junctions currently limit their application. Here, a novel, natural and simple approach to the fabrication of volumetric TI heterostructures that can overcome these core challenges is presented, using the example of a Bi_2Te_3-Te eutectic composite. The proposed method based on directional solidification of eutectic composites, enables the formation of ensembles of parallel TI-other material heterojunctions through a self-organization process. It also offers control over the heterostructures' dimensions/refinement. Electron microscopy techniques show that the heterostructure exhibits a lamellar/layered microstructure with atomically smooth Bi_2Te_3||Te interfaces. Angle-resolved photoelectron spectroscopy experiments confirm the existence of metallic surface states, while Kelvin probe force microscopy depicts the formed *p-n* junctions. The new degrees of freedom offered here, such as control of heterojunction chemical composition, packing density, and available fabrication techniques, may facilitate large-scale customized printing of topological devices.

1. Introduction

Topological insulators (TIs) are a distinguished class of materials that differ from ordinary insulators by an inverted band gap induced by strong spin-orbit interaction [1–3], present in high atomic number compounds. The high spin-orbit coupling results in an unexpected effect in TIs compared to normal insulators, namely the presence of gapless metallic boundary states, similar to the chiral edge modes in quantum Hall systems [4]. Theoretical predictions of TIs [5,6] were later followed by the experimental realization of two-dimensional (2D) TI materials with conducting edges [7] and three-dimensional (3D) TI solids with conducting surface states (SSs) [8,9]. The prototypical 3D TI materials are Bi_2Te_3, Bi_2Se_3, and Sb_2Te_3 [10,11].

TIs have great potential to be used in spintronics, faster and more efficient computing, and other areas like cutting edge detectors or magnetic devices [12,13]. However, there are several obstacles that must be overcome before integrating these materials into such applications. Firstly, a significant limitation of such systems is the masking of surface electron effects by the electrons in the bulk because of the small surface-to-volume ratio in a TI single crystal. This masking makes it difficult to exploit many phenomena and properties arising from topological SS. There are a few ways to overcome this difficulty; one aims at decreasing the free carriers in the bulk of the material by doping the TI or controlling the stoichiometry to avoid the formation of structural

* Corresponding author.
** Corresponding author at: ENSEMBLE3 Centre of Excellence, Wolczynska 133, Warsaw 01-919, Poland.
E-mail addresses: kingshuk.bandopadhyay@ensemble3.eu (K. Bandopadhyay), dorota.anna.pawlak@ensemble3.eu (D.A. Pawlak).
[1] Currently at: School of Physical Science and Technology, ShanghaiTech University, Shanghai 201210, China

https://doi.org/10.1016/j.nxmate.2024.100252
Received 13 July 2023; Received in revised form 27 March 2024; Accepted 21 May 2024
Available online 31 May 2024

defects (vacancies, antisites, etc.) creating shallow states. An alternative approach is to enhance the surface-to-volume ratio and, as a result, increase the surface carrier contribution. This effect can potentially be achieved by manufacturing heterostructures with TIs [14–16], but this is a new approach, and few such studies have been performed thus far. Secondly, TIs are highly sensitive to an air atmosphere, with the surface degrading after a few minutes of exposure and impairing the SS transport properties [17–19]. Finally, many applications require material junctions similar to, for instance, the *p-n* junctions which in traditional electronics control the flow of electrons in an electronic circuit. The ability to manufacture TI heterostructures which overcome these three obstacles, in an easy natural approach, may therefore be crucial for the effective fabrication and adaptation of TI-based devices. However, until now, heterostructures with TIs have been obtained only by costly, multistage epitaxial methods like physical vapour deposition or molecular beam epitaxy [20,21] in the form of thin films as listed in Table 1.

One of the promising approaches for the fabrication of 3D, TI composite micro-/nanostructures is based on the directional solidification of eutectic composites (ECs). During the directional solidification of a one-phase liquid, with a eutectic composition, two or more phases grow cooperatively forming natural heterostructures. Previously, ECs have been investigated mainly due to their favourable mechanical properties, such as forming strong ceramics [43]. However, recently they have been used in thermoelectric and thermophotovoltaic systems [44,45], solid-oxide fuel cells [46], photoelectrochemistry [47], photonic crystals [48], optical materials/metamaterials [49–51] and plasmonic materials [52–54]. Therefore, ECs exhibit exceptional potential for fabricating a wide variety of self-organized functional materials. There are many advantages in utilizing eutectic growth for fabrication of 3D TI heterostructures: i) almost any type of material can be used to interweave with the TI phase in the heterostructure, including semiconductors, metals, other TIs, and materials with special properties (with magnetic or electronic order, optically active, etc.); ii) the heterostructure refinement can be controlled from the micro- to the nanoscale by changing the growth rate; iii) sharp interfaces between adjacent phases can be obtained; and iv) engineering by doping, annealing or etching can also be introduced (Fig. 1**a**). This possibility of combining different phases in a eutectic heterostructure with controlled dimensions may lead to the observation of novel phenomena, such as Majorana fermions [55], magnetic proximity effects [56], giant spin-orbit coupling [57] or perhaps other hitherto unobserved proximity effects, as well as to the first structures for applications.

Here, we demonstrate a new approach for producing TI layered heterostructures in a bulk form, namely eutectic solidification from TI alloy. This approach constitutes a promising pathway towards overcoming the limitations of TIs, such as easy oxidation and the necessity of junction formation. Additionally, this method increases the surface-to-volume ratio by extending the internal surface; and the remaining volumetric sample preserves the SSs against degradation by covering every surface with a second phase. A significant advantage of the new eutectic solidification approach over top-down methods for manufacturing heterostructures is the provision of a highly-crystalline biphasic material with controllable microstructure dimensions in a single-step process. To demonstrate the potential of this approach utilizing directional solidification, we manufactured a Bi_2Te_3-Te heterostructure in which two crystalline phases are combined in a structured form with joined interfaces. The material exhibits a lamellar (layered) microstructure with atomically smooth Bi_2Te_3||Te interfaces and TI quintuplet layers parallel to the mentioned interfaces. Moreover, we report the existence of conducting SSs and the formation of p-n junctions in the obtained natural bulk eutectic heterostructure.

Table 1
Examples of topological insulator based heterostructures and fabrication methods. Abbreviations: MBE = molecular beam epitaxy, RFS = Radio Frequency Sputtering, VPD = Vapor Phase Deposition, MS = Magnetron co-Sputtering, MB = Modified Bridgman method, PLD = pulsed laser deposition.

	Type	Method	Components	Ref.
1	Thin film	MBE	Sb_2Te_3/Bi_2Te_3	[22]
2	Thin film	MBE	$(Bi_{0.5}Sb_{0.5})_2Te_3$/ $(Cr_{0.08}Bi_{0.54}Sb_{0.38})_2Te_3$	[23]
3	Thin film	MBE + RFS	Bi_2Se_3/GdN	[24]
4	Thin film	MBE	$Cr_y(Bi_xSb_{1-x})_{2-y}Te_3$/CrSb	[25]
5	Thin film	VPD	$Bi_2Te_3/Bi_2Se_3/Bi_2S_3$	[26]
6	Thin film	MBE	$(Bi,Sb)_2Te_3$/CoFeB & Bi_2Se_3/ CoFeB	[27]
7	Thin film	MBE	$(Bi_{1-x}Sb_x)_2Te_3/Cr_2Ge_2Te_6$	[28]
8	Thin film	MBE	$GeTe/Sb_2Te_3$	[29]
9	Thin film	MBE	Cr:$(Bi,Sb)_2Te_3/Cr_2O_3$	[30]
10	Thin film	MBE	$Bi_2Te_3/MnBi_2Te_4$	[31, 32]
11	Thin film	MS	Bi_2Te_3/Te	[33]
12	Thin film	MB + MBE	Bi/TlBiSe$_2$ & Bi/TlBiS$_2$	[34]
13	Thin film	MBE	$Y_3Fe_5O_{12}$/ (Bi, Sb)$_2$Te$_3$	[35]
14	Thin film	MBE	Bi_2Te_3/FeTe	[36]
15	Thin film	MBE	$(Bi_{1-x}Sb_x)_2Te_3$/InP	[37]
16	Thin film	MBE	Sb_2Te_3/V:Sb_2Te_3 & Sb_2Te_3/Cr: Sb_2Te_3	[38]
17	Thin film	Exfoliation +Dry transfer	$Cr_2Ge_2Te_6$/BiSbTeSe$_2$	[39]
18	Thin film	MBE	Bi_2Te_3/Bi_2Se_3	[40]
19	Thin film	PLD +MBE	$BaFe_{12}O_{19}/Bi_2Se_3$	[41]
20	Thin film	MBE	$(Bi,Sb)_{1.74}Cr_{0.26}Te_3/(Bi,Sb)_2Te_3$/ $(Bi,Sb)_{1.74}Cr_{0.26}Te_3$	[42]

2. Results

2.1. Growth of 3D topological insulator Bi_2Te_3-Te eutectic heterostructures

To produce a volumetric TI phase heterostructure, we chose a bismuth-tellurium system exhibiting a eutectic point at which the 3D topological insulator - Bi_2Te_3 and Te - should form a eutectic mixture (Fig. 1**b**). We directionally solidified the Bi_2Te_3-Te EC by the modified vertical Bridgman (VB) method (Fig. 2**a**) which has previously been successfully applied by us to the growth of various TI single crystals [58]. The as-grown Bi_2Te_3-Te eutectic boule inside the quartz ampoule and a sample cut perpendicular to the growth direction are shown in Fig. 2**b**. The synthesized material composed of 85 wt% Te and 15 wt% Bi, equivalent to 90 mol.% Te and 10 mol.% Bi, resulted in a mixture of 31 wt% Bi_2Te_3 and 69 wt% Te. That meant around 27% Bi_2Te_3 and 73% Te volume fractions in the grown composite.

The obtained bulk composite exhibits a layered/lamellar microstructure which is formed by the Bi_2Te_3 lamellae embedded in the Te matrix, as demonstrated by scanning electron microscopy (SEM) and energy dispersive spectroscopy (EDS) (Fig. 2**c-e**). The composition of the phases is also confirmed by the micro-Raman spectroscopy (Fig. 2**f**) and X-ray diffraction spectra (Fig. 3**b-c**). The unpolarized Raman spectra taken separately from the Bi_2Te_3 lamellae and the Te matrix, with the respective eigenpeaks, are highlighted in Fig. 2f,. The four Raman peaks of the Bi_2Te_3 layers correspond to the Raman-active oscillation modes (E_g^1 (TO), A_{1g}^1 (LO), E_g^2 (TO), A_{1g}^2 (LO)), where LO and TO correspond to longitudinal and transverse optical modes, involving quintuple layers

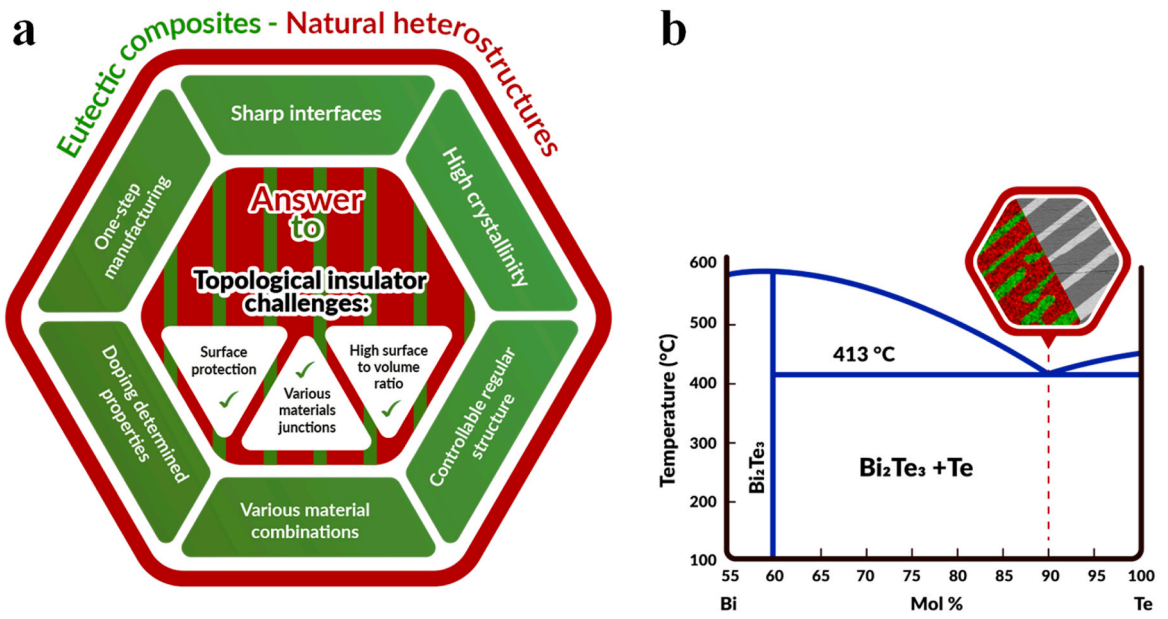

Fig. 1. Eutectic heterostructures – solution to TI challenges. (a) Advantages of ECs as natural TI heterostructures. (b) Phase diagram for the Bi_2Te_3-Te eutectic system, demonstrating one of the eutectics containing a TI phase, which is discussed in this article.

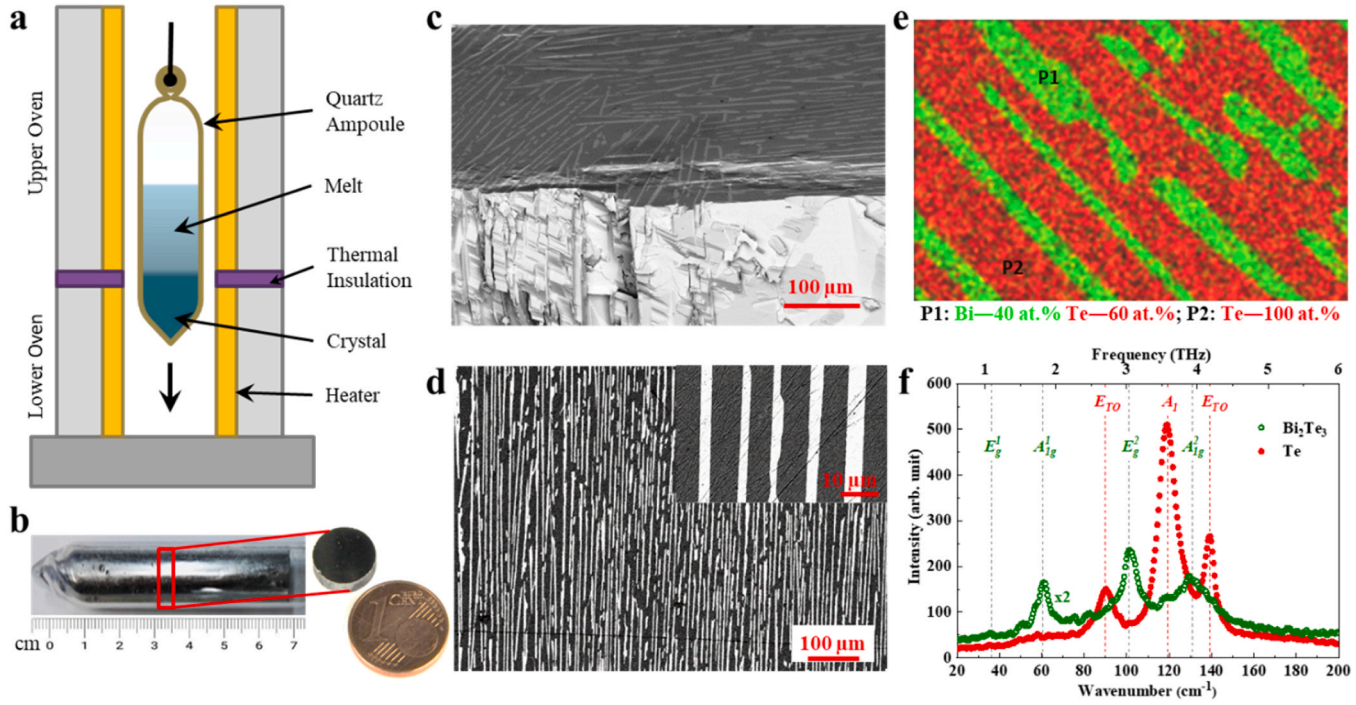

Fig. 2. Bi_2Te_3-Te TI natural eutectic heterostructure. (a) Schematic representation of the modified VB method, enabling manufacturing of volumetric ECs. (b) As-grown eutectic boule and a polished sample cut perpendicular to the growth direction. (c, d) Composite microstructure observed by scanning electron microscopy. (c) Composite, intentionally cracked to show the phase arrangement throughout the sample thickness - 45° tilted view. (d) Lamellar structure of the composite; white lamellae - Bi_2Te_3, black matrix – Te. Inset – close-up. (e, f) Phase identification on the microscale. (e) EDS map demonstrating the atomic content (red – Te, green – Bi). (f) Micro-Raman spectra of Bi_2Te_3 lamella and the Te matrix with their respective Raman-active modes. The Bi_2Te_3 spectrum was scaled by a factor of 2 for clarity.

[59]. Te, on the other hand, has three Raman-active modes: two doubly degenerate *E* modes and one nondegenerate A_1 mode [59]. These results confirm that the directional solidification of eutectics enables the production of bulk/volumetric layered TI-based heterostructures.

The eutectic micro/nanostructure can be controlled by the crystallization rate, resulting in smaller elements and shorter distances between them when applying a higher crystallization rate, according to the formula $\lambda^2 \nu = \text{const.}$ (where ν is the growth velocity and λ is the lamellar spacing) [60]. In order to prove the possibility of controlling the thickness of the TI layers in the Bi_2Te_3-Te heterostructure, we have grown these materials applying different pulling rates (from ~1.2 mm/h to 20 mm/h). In the micro-pulling down method, pulling rates correspond to the crystallization rates of the grown material. We tuned the width of the Bi_2Te_3 layers from ~85 µm to < 1µm and their separation

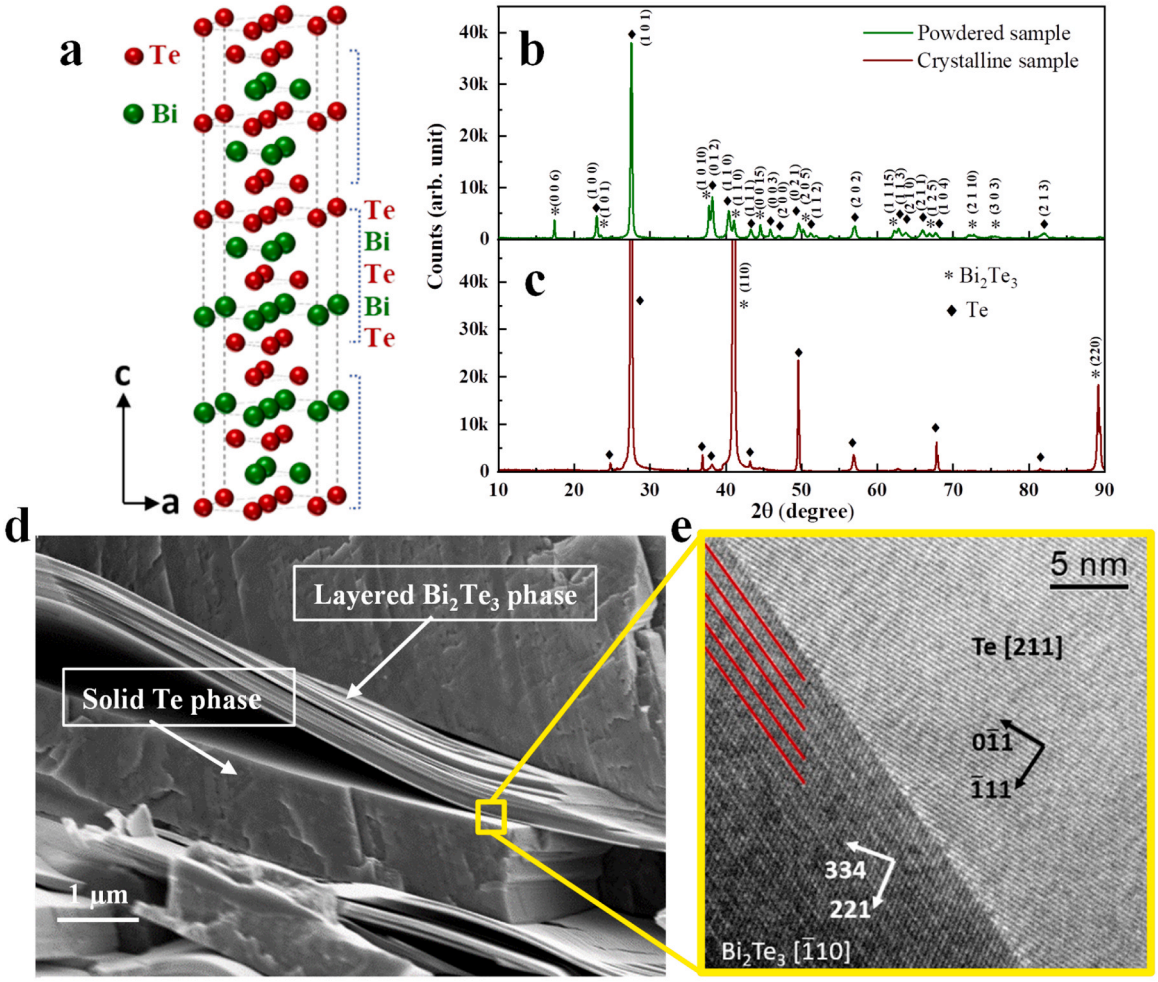

Fig. 3. Sharp, atomically smooth, ||-to-Bi_2Te_3 quintuplets interfaces between Bi_2Te_3 and Te lamellae in the Bi_2Te_3-Te eutectic heterostructure. (a) Visualization of the Bi_2Te_3 layered crystal structure formed by Te-Bi-Te-Bi-Te quintuplets. (b, c) Identification of (b) phases and (c) their growth direction by X-ray diffraction demonstrating single orientation for the Bi_2Te_3 phase. (d) SEM image of a cracked sample demonstrating the layered structure of the Bi_2Te_3 phase and smooth boundaries between phases. (e) HRTEM image of the Te||Bi_2Te_3 interface. Visible quintuplet layers are parallel to the interface, marked in red.

distance in the Te matrix from ~180 μm to ~4 μm (Supplementary Table 1). By varying the growth rate further, the microstructure of the TI phases containing the eutectic could be controlled to a much larger extent, as has been shown for other ECs [61].

2.2. *Atomically smooth Bi_2Te_3||Te interfaces*

Bi_2Te_3 has a layered structure which is formed by Te-Bi-Te-Bi-Te sheets [62] called quintuple layers (quintuplets) and it crystallizes in the rhombohedral structure with the $D_{3d}^5 - R\bar{3}m$ space group (Fig. 3**a**). The planar, covalently bonded quintuplets are held together by weak van der Waals interactions along the c axis of the hexagonal lattice, so the Bi_2Te_3 crystal can be easily exfoliated along the top or bottom quintuplet Te layer, thus perpendicular to the c axis [63].

The growth of the Bi_2Te_3 phase in the Bi_2Te_3-Te heterostructure is distinct in the [110] direction, as demonstrated by X-ray diffraction of the sample cut perpendicular to the growth direction (Fig. 3**c**). For the Te phase, in contrast, more than one growth orientation is observed (Fig. 3c); but [101] is the dominant orientation. The Bi_2Te_3 [110] crystal direction is perpendicular to the c axis, which is consistent with our observation that exfoliation in the Bi_2Te_3-Te composite occurs only parallel to the crystal growth direction. The tendency for exfoliation can be seen at the surface, especially for the cracked perpendicular-to-the-growth direction sample (Fig. 3**d**), as observed with SEM. The layered structure of the eutectic with the layered Bi_2Te_3 phase partly exfoliated from the Te phase during cracking is revealed. The Bi_2Te_3-Te eutectic heterostructure also exhibits atomically smooth Bi_2Te_3||Te interfaces (Fig. 3**e**) with the quintuplet layers perfectly parallel to them, as revealed by high-resolution transmission electron microscopy (HRTEM). The atomically smooth interface here is a combined result of the natural eutectic tendency for sharp interfaces between adjacent phases of an EC and the layered structure of the TI resulting from the quintuplets. This explains the fact that exfoliation occurs only along the growth direction, as the quintuplets lay parallel to it. Additionally, at the interfaces, no precipitates or discontinuities are exposed, which is essential for the investigation of the proximity effects [34]. In summary: we have shown in the obtained Bi_2Te_3 heterostructures: (i) an atomically smooth Bi_2Te_3||Te interface; (ii) TI quintuplets parallel to Bi_2Te_3||Te interface; (iii) that the Bi_2Te_3||Te interface is perpendicular to Bi_2Te_3 c-axis, which is normally the exfoliated TI surface. Consequently, the typically investigated TI surface is here protected by the adjacent phase. Thus, when used in spintronic devices, the polarized spin current [64] could flow along the heterostructure interfaces and hence be shielded from atmospheric effects.

2.3. *Surface states in Bi_2Te_3-Te heterostructure*

Having understood the stoichiometry of the obtained heterostructure, in the next step we needed to confirm that the metallic surface states are preserved within the Bi_2Te_3 phase, which is commonly

realized using an angle-resolved photoemission spectroscopy (ARPES). In our case, micro-angle-resolved photoemission spectroscopy (μARPES) measurements were essential to study the SSs due to the micron-sized TI Bi_2Te_3 lamellas. The sample was cleaved under vacuum along the growth direction of the Bi_2Te_3 phase to expose an oxidation-free surface for the measurement. By using the core level of Bi ($5d_{3/2}/5d_{5/2}$), the bright Bi_2Te_3 layers could be easily distinguished from the Te matrix in the real-space mapping, as shown in Supplementary Figure S1. Thus using μARPES, the area of interest which is the Bi_2Te_3 could easily be distinguished to study the surface states of the TI. The 3D spectral intensity plot in (k_x, k_y, E) space (Fig. 4**a**) probed on the Bi_2Te_3 lamellae illustrates, as usual, the bulk band dispersions: the bulk conduction band (BCB) and bulk valence band (BVB). Additionally, the topological SS with Dirac band structure is observed, confirming the topological nature of the material. The high symmetry cut of the surface Brillouin zone, Fig. 4**b**, and the constant energy contours, Fig. 4**c-d**, clearly reveal the evolution of the band structure with the change of the binding energy. The obtained results match well with the previously reported data for the Bi_2Te_3 single crystal [11]. Notably, the low quality of the band structure is a result of the sacrifice in the energy resolution in the high spatially resolved μARPES measurement, which was necessary to take the measurements of the micron-scale Bi_2Te_3 precipitates. In summary, we have proven that the topological surface states are preserved in the obtained material.

2.4. *p-n junctions at Bi_2Te_3||Te interfaces*

An additional important aspect for TI-based devices is the ability to form various heterojunctions which will enable control over the transport of spin and charge. For instance, formation of junctions with ferromagnetic material or a *p-n/Schottky* junction is necessary in order to control spin or charge transport, respectively [65]. It can be noticed in the ARPES spectrum of the Bi_2Te_3 lamellae, Fig. 4a, that the '0' binding energy level, which represents the Fermi level, crosses the conduction band. This means that the Bi_2Te_3 lamellae have a *n*-type nature. On the other hand, to check the electronic nature of the Te matrix, the current-voltage (*I-V*) characteristics using conductive atomic force microscopy (CAFM) have been obtained (Supplementary Figure S2). When a positive bias is applied to the sample, the *Te-AFM tip* junction starts conducting; but with a negative bias, it does not. That clearly shows that the Te matrix behaves as a p-type semiconductor with the rectifying behaviour of a Schottky junction. To understand the band alignment, we used Kelvin probe force microscopy (KPFM), an effective tool that allows the determination of junction properties with high spatial resolution. KPFM measures the contact potential difference (CPD) between a conducting AFM tip and a sample, which is induced based on the difference between the work functions of the metal tip and the sample surface. The work functions of the materials is the most important aspect to understand the potential of them in future electronic devices. In the 3D plot of the CPD (Fig. 5**a**), we observe a sharp contrast between the *p*-type (dark) and *n*-type (bright) regions, correlated with the Te matrix and Bi_2Te_3 lamellae, respectively. The CPD value increases from the *p*- to the *n*-type phase following the fact that in our experiment, the compensating DC bias that induces the CPD is applied to the tip [66]. The real work function of the materials was calculated from the CPD values and is plotted in Fig. 5**b**, using tip work function (ϕ_{tip}) = 4.7 *eV* as an offset. In the absence of surface band bending, the difference in the potentials between the *n*- and *p*-sides corresponds to the built-in potential (V_{bi}), which is ~ 0.11 V in the present case. The diffusion of charges near the junction builds up the depletion region, the width of which varies from 1.5 to 2 μm, obtained from the experimental data by fitting the potential profile with a sigmoid curve. Since the KPFM measurements have been performed in air, the measured values may vary from the real one due to the oxidation of the surfaces. While the conclusive evidence for the formation of p-n junction is to show the diode rectification across the single interface using micron-scale transport measurement, in the present study we take the sigmoidal curve as evidence for the formation of the p-n junction between the Te and Bi_2Te_3 phases. The positions of the Fermi energies of the materials with respect to vacuum and the formation of the *p-n* junction are illustrated in Fig. 5**c**. Thus we have demonstrated that using directional solidification of eutectic composites, functional heterojunctions of TI materials can be produced to be readily used in future topological electronic devices.

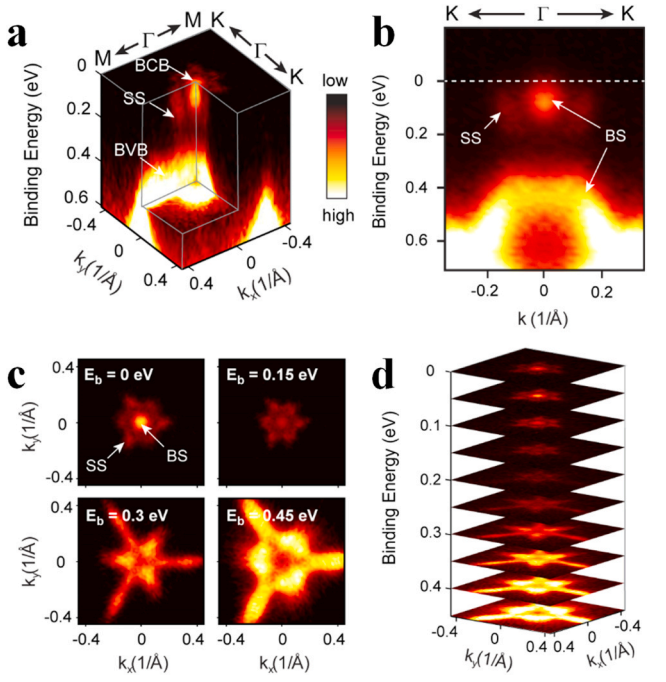

Fig. 4. Surface states (SSs) in the Bi_2Te_3-Te eutectic heterostructure observed by μARPES. (a) Band structure probed on the Bi_2Te_3 lamellae with a photon energy of 74 eV, illustrating the dispersions of the topological SSs, bulk conduction band (BCB) and bulk valence band (BVB). (b) High symmetry cut of the band dispersions along the K-Γ-K direction, clearly revealing the gapped bulk state and the Dirac-cone shape of the topological SS in the gap. (c) Constant energy contours extracted at different binding energies from the full ARPES mapping, showing the evolution of the band structure. (d) Slice plot of the constant energy contours.

3. Discussion and outlook

In conclusion, eutectic natural heterostructures can provide an answer to several issues which formerly prevented the use of TIs in applications. The example of the Bi_2Te_3-Te EC revealed that we have obtained a volumetric topological insulator heterostructure: (i) with many parallel TI layers embedded in another phase; (ii) with atomically sharp interfaces between these two phases along with the quintuplet layers parallel to the interfaces; and (iii) with a micro/nanostructure refinement controlled by the growth rate (i.e. for Bi_2Te_3-Te EC applied slow pulling rate of 1.2–20 mm/h resulted in 90 μm – 700 nm width of the Bi_2Te_3 lamellae).

Such a multilayered structure increases the surface-to-volume electron concentration ratio, while the surface states are protected at the TI|| (other material) interfaces. The atomically sharp interfaces with the quintuplets parallel to them could enable applications as well as observation of proximity effects. Gapless SSs should exist at any surface of the TI [67]; thus, the occurrence of dissipationless transport of electrons with ordered spins is expected at the solid-solid interfaces in the eutectic heterostructures. We have shown that the combination of a TI with another material through eutectic transition enables the development of novel three-dimensional (3D), standalone, self-organized TI heterostructures such as materials with the following properties: (i) a

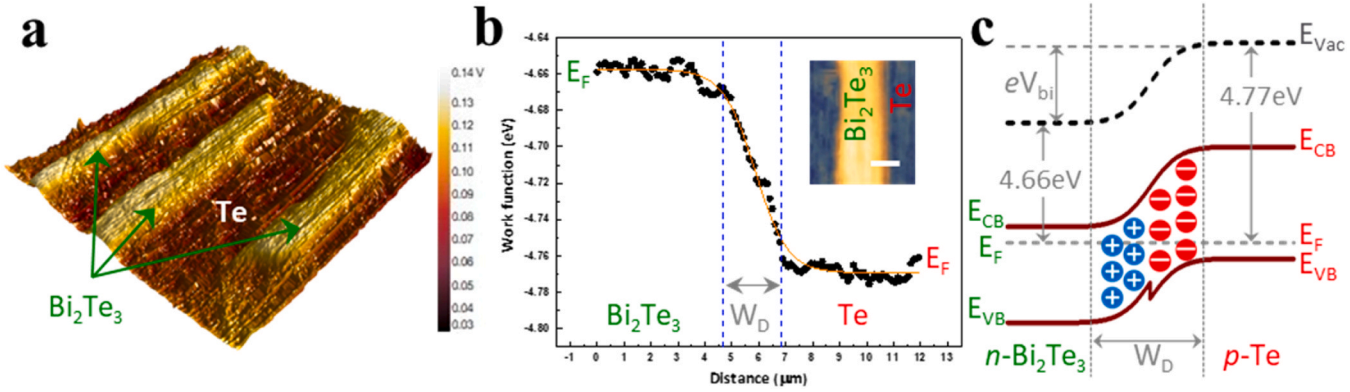

Fig. 5. KPFM study of the *p-n* junction in the Bi_2Te_3(*n*)–Te(*p*) eutectic heterostructure. (a) 3D CPD profile showing the surface potential of the Te matrix with a darker contrast, exhibiting an ~110 mV lower value with respect to the Bi_2Te_3 lamellae. (b) Change in the work function along the Bi_2Te_3-Te junction showing the absolute position of the Fermi energies in the lamellae and matrix. The inset shows the 2D CPD plot of the heterostructure with the area where the line profile was taken indicated as a white line. The orange line is a fit to a sigmoid curve. The profile also shows how the surface potential changes along the depletion width (W_D). (c) Schematic electronic band structure of the *p-n* junction formed at the Bi_2Te_3-Te interface (not to scale). The absolute positions of the Fermi energy (E_F) levels with respect to the vacuum energy (E_{Vac}) levels are shown along with the built-in potential (V_{bi}) of the junction.

high surface-to-volume ratio; (ii) favourable gapless topological surfaces protected against air exposure by a second phase; and (iii) the ability to forming heterojunctions. This approach can be used for various material combinations as long as they form a eutectic mixture.

Several unusual properties can arise due to the control of multiple interfaces by altering the second phase material, which can be an ordinary semiconductor, insulator, metal, superconductor, ferromagnet, antiferromagnet or other kind of material. These unique properties might include unusual phenomena such as massive Dirac fermions [68], exotic Majorana states [55] and the creation of an ideal thermoelectric material [15]. In principle, eutectic materials can be grown in the form of bulk, layers as well as being printed and sprayed. Notably, the eutectic geometry can also be engineered during the growth. For example, by applying rotation, straight lamellae/layers/interfaces can be turned into curved lamellae/layers/interfaces [69]; and changes in the geometry can be induced by growing the material inside a periodic template [70]. ECs can also be engineered after growth by etching the non-TI phase and covering the remaining expanded surface with other materials, as shown for other ECs [49,71]. This might also enable the production of material junctions that do not form eutectic mixtures. Owing to new technological developments such as direct EC ink writing [72], spintronic device printing based on TI eutectic heterostructures could be an avenue for future studies. Up to now, TI heterostructures were obtained only by top-down methods including physical vapour deposition and molecular beam epitaxy [20,21], where these kinds of engineering methods and such wide material combinations are not available.

4. Methods

4.1. Synthesis

The Bi_2Te_3-Te eutectic was grown by a modified vertical Bridgman method (VB) in a vacuum-sealed quartz ampoule according to the binary phase diagram described in Abrikosov *et al.* [73] The structure of the eutectic was controlled by the pulling rate and by adjusting the diameter of the ampoule. The starting materials, bismuth (Bi) chunks and tellurium (Te) granules (Sigma-Aldrich) of 5N5 purity were sealed in a quartz ampoule under ~ 10^{-5} mbar vacuum. To avoid inhomogeneity in initial mixture, which can lead to localized variations in composition, the ampoule was heated above 450 °C and was shaken to achieve uniform distribution of components. After achieving homogeneous melting of the material, the ampoule was pulled to the lower temperature region of the furnace at a constant rate. Volumetric boules of eutectic composites with different microstructure refinements were obtained by varying the pulling rate.

4.2. Scanning electron microscopy (SEM) and energy dispersive spectroscopy (EDS)

SEM and EDS measurements were performed on an AURIGA 60 CrossBeam Workstation from Carl Zeiss. SEM images were collected using both secondary and backscattered electron detectors at different electron accelerating voltages.

4.3. Micro-Raman spectroscopy

Raman spectra were collected at room temperature by means of a LabRAM HR Evolution spectrometer (Horiba Jobin Yvon) equipped with an Olympus BXFM-ILHS confocal microscope working in the backscattering geometry, using a 532 nm excitation laser source (Nd:YAG laser, Torus Laser, Laser Quantum, U.K.). Measurements were performed over the spectral range of 20–200 cm^{-1}; the scattered signal was acquired with a 100x objective (NA = 0.9); the diameter of the confocal hole was 200 μm; and the diffraction grating was 1800 lines/mm. In the mapping mode, the spectra were acquired with an accumulation time of 10 s and three measurements were averaged.

4.4. High-resolution transmission electron microscopy (HRTEM)

HRTEM measurements were performed using a 300 kV JEM 3010 Ultrahigh Resolution Analytical Electron Microscope from JEOL.

4.5. X-ray diffraction (XRD) spectroscopy

XRD data were collected with use of a Rigaku SmartLab® 3 kW powder X-ray diffractometer, with reference radiation of Cu K_α = 1.540 Å at an operating voltage of 40 kV, and analysed using the PDF4+ 2018 database. A mechanically-polished crystalline sample was used to analyse the crystal plane directions with respect to the composite growth direction. A freshly cut sample was ground using a mortar to investigate the presence of all the phases in the composite.

4.6. Micro-angle-resolved photoemission spectroscopy (μ-ARPES)

μ-ARPES measurements were carried out at the end station of the SpectroMicroscopy-beamline 3.2 L of the Elettra Synchrotron Light Source utilizing a 74 eV photon beam. The size of the beam was focused down to 1 μm by using the multilayer coated optics from Schwarzschild

objectives. The overall energy and angular resolutions were 50 meV and 1°, respectively. The sample was kept in a vacuum of 1×10^{-10} mbar with a temperature of 100 K during the measurement. A ceramic rod was used to cleave the sample inside the chamber to expose a fresh surface.

4.7. Kelvin probe force microscopy (KPFM)

A CombiScope™-1000SPM from AIST-NT was used for KPFM measurement. An Au-coated cantilever from μ-Masch (HQ:NSC14/CR-AU, ~5 N m^{-1} force constant, resonance frequency ~160 kHz) was used for the experiment. Topography measurements were carried out in semi-contact mode using the oscillation amplitude as a feedback parameter. The measurement of the contact potential difference (CPD) between the tip and sample proceeded in noncontact mode (the tip-sample distance was maintained at 30 nm) by applying a fixed AC voltage of 4 V at 154 kHz to the atomic force microscopy (AFM) tip while the sample was held at ground potential. A second feedback was used to adjust the DC bias between the tip and sample to nullify the electrostatic interaction between them, in order to determine the CPD (amplitude modulation mode). To calibrate the work function of our Au-coated cantilever, a highly oriented pyrolytic graphite (HOPG) freshly cleaved in ambient atmosphere was used as the reference sample. Previous work has reported that the work function of HOPG immediately after cleavage in air is $\phi_{HOPG} = (4.475 \pm 0.005)$ eV [74]. Measurements of the reference HOPG sample using the Au-coated cantilever found $\Delta\phi_{HOPG} = \phi_{HOPG} - \phi_{tip} \sim 0.23\ eV$, corresponding to $\phi_{tip} = 4.7\ eV$, in agreement with earlier works [74] on the work function of Au in air.

CRediT authorship contribution statement

Kingshuk Bandopadhyay: Conceptualization, Methodology, Formal analysis, Investigation, Visualization, Writing - Original Draft, Writing - Review & Editing
Marta Buza: Conceptualization, Methodology, Formal analysis, Investigation, Writing - Original Draft
Cheng Chen: Investigation, Visualization, Formal analysis
Andrzej Materna: Investigation
Kamil Szlachetko: Investigation
Piotr Piotrowski: Investigation
Hańcza B. Surma: Investigation, Writing - Original Draft
Jolanta Borysiuk: Investigation
Ryszard Diduszko: Investigation
Alexei Barinov: Investigation
Yulin L. Chen: Validation
Maria Kaminska: Validation, Supervision, Writing - Review & Editing
Dorota A. Pawlak: Conceptualization, Methodology, Resources, Visualization, Supervision, Writing - Review & Editing, Project administration, Funding acquisition

Declaration of Competing Interest

The authors declare the following financial interests/personal relationships which may be considered as potential competing interests: The authors have applied for patent regarding this work. Patent no. EP2318815.7 & P.445712

Acknowledgements

The authors thank ENSEMBLE [3] Project (MAB/2020/14) which is carried out within the International Research Agendas Programme (IRAP) of the Foundation for Polish Science co-financed by the European Union under the European Regional Development Fund and Teaming (GA. No. 857543) Horizon 2020 programme of the European Commission; the TEAM/2016–3/29 Grant within the TEAM program of the Foundation for Polish Science co-financed by the European Union under the European Regional Development Fund; and the HARMONIA Project (2013/10/M/ST5/00650) from the National Science Centre.

Additional Information

This paper is dedicated to the memory of our colleague and friend Hańcza Barbara Surma.

Appendix A. Supporting information

Supplementary data associated with this article can be found in the online version at doi:10.1016/j.nxmate.2024.100252.

References

[1] J.E. Moore, The birth of topological insulators, Nature *464* (2010) 194–198, https://doi.org/10.1038/nature08916.
[2] L. Fu, C.L. Kane, E.J. Mele, Topological insulators in three dimensions, Phys. Rev. Lett. *98* (2007) 106803, https://doi.org/10.1103/PhysRevLett.98.106803.
[3] B.A. Bernevig, T.L. Hughes, S.C. Zhang, Quantum spin Hall effect and topological phase transition in HgTe quantum wells, Science *314* (2006) 1757–1761, https://doi.org/10.1126/science.1133734.
[4] J.E. Moore, L. Balents, Topological invariants of time-reversal-invariant band structures, Phys. Rev. B *75* (2007), https://doi.org/10.1103/PhysRevB.75.121306.
[5] B.A. Volkov, O.A. Pankratov, Two-dimensional massless electrons in an inverted contact, Sov. J. Exp. Theor. Phys. Lett. *42* (1985) 178.
[6] C.L. Kane, E.J. Mele, Quantum spin Hall effect in graphene, Phys. Rev. Lett. *95* (2005) 226801, https://doi.org/10.1103/PhysRevLett.95.226801.
[7] M. König, S. Wiedmann, C. Brüne, A. Roth, H. Buhmann, L.W. Molenkamp, X.-L. Qi, S.-C. Zhang, Quantum spin hall insulator state in HgTe quantum wells, Science *318* (2007) 766, https://doi.org/10.1126/science.1148047.
[8] D. Hsieh, D. Qian, L. Wray, Y. Xia, Y.S. Hor, R.J. Cava, M.Z. Hasan, A topological Dirac insulator in a quantum spin Hall phase, Nature *452* (2008) 970–974, https://doi.org/10.1038/nature06843.
[9] D. Hsieh, Y. Xia, L. Wray, D. Qian, A. Pal, J.H. Dil, J. Osterwalder, F. Meier, G. Bihlmayer, C.L. Kane, et al., Observation of unconventional quantum spin textures in topological insulators, Science *323* (2009) 919, https://doi.org/10.1126/science.1167733.
[10] H. Zhang, C.-X. Liu, X.-L. Qi, X. Dai, Z. Fang, S.-C. Zhang, Topological insulators in Bi_2Se_3, Bi_2Te_3 and Sb_2Te_3 with a single Dirac cone on the surface, NatPh *5* (2009) 438–442, https://doi.org/10.1038/nphys1270.
[11] Y.L. Chen, J.G. Analytis, J.H. Chu, Z.K. Liu, S.K. Mo, X.L. Qi, H.J. Zhang, D.H. Lu, X. Dai, Z. Fang, et al., Experimental realization of a three-dimensional topological insulator, Bi_2Te_3, Science *325* (2009) 178–181, https://doi.org/10.1126/science.1173034.
[12] D. Pesin, A.H. MacDonald, Spintronics and pseudospintronics in graphene and topological insulators, Nat. Mater. *11* (2012) 409–416, https://doi.org/10.1038/nmat3305.
[13] M. He, H. Sun, Q.L. He, Topological insulator: Spintronics and quantum computations, Front. Phys. *14* (2019), https://doi.org/10.1007/s11467-019-0893-4.
[14] T. Hesjedal, Y. Chen, Topological insulators: engineered heterostructures, Nat. Mater. *16* (2016) 3–4, https://doi.org/10.1038/nmat4835.
[15] D. Kong, Y. Cui, Opportunities in chemistry and materials science for topological insulators and their nanostructures, Nat. Chem. *3* (2011) 845–849, https://doi.org/10.1038/nchem.1171.
[16] H. Peng, W. Dang, J. Cao, Y. Chen, D. Wu, W. Zheng, H. Li, Z.X. Shen, Z. Liu, Topological insulator nanostructures for near-infrared transparent flexible electrodes, Nat. Chem. *4* (2012) 281–286, https://doi.org/10.1038/nchem.1277.
[17] D. Kong, J.J. Cha, K. Lai, H. Peng, J.G. Analytis, S. Meister, Y. Chen, H.-J. Zhang, I. R. Fisher, Z.-X. Shen, Y. Cui, Rapid surface oxidation as a source of surface degradation factor for Bi_2Se_3, ACS Nano *5* (2011) 4698–4703, https://doi.org/10.1021/nn200556h.
[18] C.R. Thomas, M.K. Vallon, M.G. Frith, H. Sezen, S.K. Kushwaha, R.J. Cava, J. Schwartz, S.L. Bernasek, Surface oxidation of $Bi_2(Te,Se)_3$ topological insulators depends on cleavage accuracy, Chem. Mater. *28* (2016) 35–39, https://doi.org/10.1021/acs.chemmater.5b03923.
[19] H. Tay, Y.-F. Zhao, L.-J. Zhou, R. Zhang, Z.-J. Yan, D. Zhuo, M.H.W. Chan, C.-Z. Chang, Environmental doping-induced degradation of the quantum anomalous hall insulators, Nano Lett. *23* (2023) 1093–1099, https://doi.org/10.1021/acs.nanolett.2c04871.
[20] S.K. Chong, K.B. Han, A. Nagaoka, R. Tsuchikawa, R. Liu, H. Liu, Z.V. Vardeny, D. A. Pesin, C. Lee, T.D. Sparks, V.V. Deshpande, Topological insulator-based van der waals heterostructures for effective control of massless and massive dirac fermions, Nano Lett. *18* (2018) 8047–8053, https://doi.org/10.1021/acs.nanolett.8b04291.
[21] A. Richardella, A. Kandala, N. Samarth, Topological insulator thin films and heterostructures: epitaxial growth, transport, and magnetism, Topol. Insul. (2015) 295–329, https://doi.org/10.1002/9783527681594.ch12.
[22] M. Eschbach, E. Mlynczak, J. Kellner, J. Kampmeier, M. Lanius, E. Neumann, C. Weyrich, M. Gehlmann, P. Gospodaric, S. Doring, et al., Realization of a vertical topological p-n junction in epitaxial Sb_2Te_3/Bi_2Te_3 heterostructures, Nat. Commun. *6* (2015) 8816, https://doi.org/10.1038/ncomms9816.

[23] Y. Fan, P. Upadhyaya, X. Kou, M. Lang, S. Takei, Z. Wang, J. Tang, L. He, L. T. Chang, M. Montazeri, et al., Magnetization switching through giant spin-orbit torque in a magnetically doped topological insulator heterostructure, Nat. Mater. *13* (2014) 699–704, https://doi.org/10.1038/nmat3973.

[24] A. Kandala, A. Richardella, D.W. Rench, D.M. Zhang, T.C. Flanagan, N. Samarth, Growth and characterization of hybrid insulating ferromagnet-topological insulator heterostructure devices, Appl. Phys. Lett. *103* (2013) 202409, https://doi.org/10.1063/1.4831987.

[25] P. Liu, C. Eckberg, L. Pan, P. Zhang, K.L. Wang, G. Lupke, Ultrafast optical control of surface and bulk magnetism in magnetic topological insulator/antiferromagnet heterostructure, Sci. Rep. *12* (2022) 12117, https://doi.org/10.1038/s41598-022-16205-3.

[26] C. Lu, M. Luo, W. Dong, Y. Ge, T. Han, Y. Liu, X. Xue, N. Ma, Y. Huang, Y. Zhou, X. Xu, Bi(2) Te(3) /Bi(2) Se(3) /Bi(2) S(3) cascade heterostructure for fast-response and high-photoresponsivity photodetector and high-efficiency water splitting with a small bias voltage, Adv. Sci. (Weinh.) *10* (2023) e2205460, https://doi.org/10.1002/advs.202205460.

[27] Y. Lv, J. Kally, D. Zhang, J.S. Lee, M. Jamali, N. Samarth, J.P. Wang, Unidirectional spin-Hall and Rashba-Edelstein magnetoresistance in topological insulator-ferromagnet layer heterostructures, Nat. Commun. *9* (2018) 111, https://doi.org/10.1038/s41467-017-02491-3.

[28] M. Mogi, K. Yasuda, R. Fujimura, R. Yoshimi, N. Ogawa, A. Tsukazaki, M. Kawamura, K.S. Takahashi, M. Kawasaki, Y. Tokura, Current-induced switching of proximity-induced ferromagnetic surface states in a topological insulator, Nat. Commun. *12* (2021) 1404, https://doi.org/10.1038/s41467-021-21672-9.

[29] H. Nakamura, J. Hofmann, N. Inoue, S. Koelling, P.M. Koenraad, G. Mussler, D. Grutzmacher, V. Narayan, Probing embedded topological modes in bulk-like GeTe-Sb(2)Te(3) heterostructures. Sci. Rep. *10* (2020) 21806 https://doi.org/10.1038/s41598-020-76885-7.

[30] L. Pan, A. Grutter, P. Zhang, X. Che, T. Nozaki, A. Stern, M. Street, B. Zhang, B. Casas, Q.L. He, et al., Observation of quantum anomalous hall effect and exchange interaction in topological insulator/antiferromagnet heterostructure, Adv. Mater. *32* (2020) e2001460, https://doi.org/10.1002/adma.202001460.

[31] E.D.L. Rienks, S. Wimmer, J. Sanchez-Barriga, O. Caha, P.S. Mandal, J. Ruzicka, A. Ney, H. Steiner, V.V. Volobuev, H. Groiss, et al., Large magnetic gap at the Dirac point in Bi2Te3/MnBi2Te4 heterostructures, Nature *576* (2019) 423–428, https://doi.org/10.1038/s41586-019-1826-7.

[32] H. Deng, Z. Chen, A. Wołoś, M. Konczykowski, K. Sobczak, J. Sitnicka, I. V. Fedorchenko, J. Borysiuk, T. Heider, Ł. Pluciński, et al., High-temperature quantum anomalous Hall regime in a MnBi2Te4/Bi2Te3 superlattice, NatPh *17* (2020) 36–42, https://doi.org/10.1038/s41567-020-0998-2.

[33] H.-J. Shang, F.-Z. Ding, Y. Deng, H. Zhang, Z.-B. Dong, W.-J. Xu, D.-X. Huang, H.-W. Gu, Z.-G. Chen, Highly (00l)-oriented Bi2Te3/Te heterostructure thin films with enhanced power factor, Nanoscale *10* (2018) 20189–20195, https://doi.org/10.1039/c8nr07112h.

[34] T. Shoman, A. Takayama, T. Sato, S. Souma, T. Takahashi, T. Oguchi, K. Segawa, Y. Ando, Topological proximity effect in a topological insulator hybrid, Nat. Commun. *6* (2015) 6547, https://doi.org/10.1038/ncomms7547.

[35] H. Wang, J. Kally, J.S. Lee, T. Liu, H. Chang, D.R. Hickey, K.A. Mkhoyan, M. Wu, A. Richardella, N. Samarth, Surface-state-dominated spin-charge current conversion in topological-insulator-ferromagnetic-insulator heterostructures, Phys. Rev. Lett. *117* (2016) 076601, https://doi.org/10.1103/PhysRevLett.117.076601.

[36] K. Yasuda, H. Yasuda, T. Liang, R. Yoshimi, A. Tsukazaki, K.S. Takahashi, N. Nagaosa, M. Kawasaki, Y. Tokura, Nonreciprocal charge transport at topological insulator/superconductor interface, Nat. Commun. *10* (2019) 2734, https://doi.org/10.1038/s41467-019-10658-3.

[37] R. Yoshimi, A. Tsukazaki, K. Kikutake, J.G. Checkelsky, K.S. Takahashi, M. Kawasaki, Y. Tokura, Dirac electron states formed at the heterointerface between a topological insulator and a conventional semiconductor, Nat. Mater. *13* (2014) 253–257, https://doi.org/10.1038/nmat3885.

[38] F. Wang, X. Wang, Y.-F. Zhao, D. Xiao, L.-J. Zhou, W. Liu, Z. Zhang, W. Zhao, M.H. W. Chan, N. Samarth, et al., Interface-induced sign reversal of the anomalous Hall effect in magnetic topological insulator heterostructures, Nat. Commun. *12* (2021), https://doi.org/10.1038/s41467-020-20349-z.

[39] A.E. Llacsahuanga Allcca, X.C. Pan, I. Miotkowski, K. Tanigaki, Y.P. Chen, Gate-tunable anomalous hall effect in stacked van der waals ferromagnetic insulator-topological insulator heterostructures, Nano Lett. *22* (2022) 8130–8136, https://doi.org/10.1021/acs.nanolett.2c02571.

[40] T. Sato, K. Sugawara, T. Kato, Y. Nakata, S. Souma, K. Yamauchi, T. Oguchi, T. Takahashi, T. Sato, Manipulation of dirac cone in topological insulator/topological insulator heterostructure, ACS Appl. Electron. Mater. *3* (2021) 1080–1085, https://doi.org/10.1021/acsaelm.0c00918.

[41] P. Li, J. Ding, S.S.L. Zhang, J. Kally, T. Pillsbury, O.G. Heinonen, G. Rimal, C. Bi, A. DeMann, S.B. Field, et al., Topological hall effect in a topological insulator interfaced with a magnetic insulator, Nano Lett. *21* (2020) 84–90, https://doi.org/10.1021/acs.nanolett.0c03195.

[42] Y.F. Zhao, R. Zhang, J. Cai, D. Zhuo, L.J. Zhou, Z.J. Yan, M.H.W. Chan, X. Xu, C. Z. Chang, Creation of chiral interface channels for quantized transport in magnetic topological insulator multilayer heterostructures, Nat. Commun. *14* (2023) 770, https://doi.org/10.1038/s41467-023-36488-y.

[43] Y. Waku, N. Nakagawa, T. Wakamoto, H. Ohtsubo, K. Shimizu, Y. Kohtoku, A ductile ceramic eutectic composite with high strength at 1,873 K, Nature *389* (1997) 49–52, https://doi.org/10.1038/37937.

[44] G.J. Snyder, E.S. Toberer, Complex thermoelectric materials, Nat. Mater. *7* (2008) 105–114, https://doi.org/10.1038/nmat2090.

[45] D. Sola, P.B. Oliete, R.I. Merino, J.I. Peña, Directionally solidified Ni doped MgO-MgSZ eutectic composites for thermophotovoltaic devices, J. Eur. Ceram. Soc. *39* (2019) 1206–1213, https://doi.org/10.1016/j.jeurceramsoc.2018.12.032.

[46] R.I. Merino, J.I. Peña, V.M. Orera, Compositionally graded YSZ–NiO composites by surface laser melting, J. Eur. Ceram. Soc. *30* (2010) 147–152, https://doi.org/10.1016/j.jeurceramsoc.2009.04.031.

[47] K. Kolodziejak, J. Sar, K. Wysmulek, P. Osewski, M. Warczak, A. Sadkowski, M. Radecka, D.A. Pawlak, When eutectic composites meet photoelectrochemistry – Highly stable and efficient UV–visible hybrid photoanodes, J. Catal. *352* (2017) 93–101, https://doi.org/10.1016/j.jcat.2017.04.019.

[48] J. Kim, L.K. Aagesen, J.H. Choi, J. Choi, H.S. Kim, J. Liu, C.R. Cho, J.G. Kang, A. Ramazani, K. Thornton, P.V. Braun, Template-directed directionally solidified 3d mesostructured AgCl-KCl eutectic photonic crystals, Adv. Mater. *27* (2015) 4551–4559, https://doi.org/10.1002/adma.201502265.

[49] D.A. Pawlak, S. Turczynski, M. Gajc, K. Kolodziejak, R. Diduszko, K. Rozniatowski, J. Smalc, I. Vendik, How far are we from making metamaterials by self-organization? The microstructure of highly anisotropic particles with an SRR-like geometry. Adv. Funct. Mater. *20* (2010) 1116–1124, https://doi.org/10.1002/adfm.200901875.

[50] P. Osewski, A. Belardini, M. Centini, C. Valagiannopoulos, G. Leahu, R. Li Voti, M. Tomczyk, A. Alù, D.A. Pawlak, C. Sibilia, New self-organization route to tunable narrowband optical filters and polarizers demonstrated with ZnO–$ZnWO_4$ eutectic composite, Adv. Opt. Mater. *8* (2020) 1901617, https://doi.org/10.1002/adom.201901617.

[51] E. Petronijevic, M. Tomczyk, A. Belardini, P. Osewski, P. Piotrowski, M. Centini, G. Leahu, R.L. Voti, D.A. Pawlak, C. Sibilia, M.C. Larciprete, Surprising eutectics: enhanced properties of ZnO-ZnWO(4) from visible to MIR, Adv. Mater. (2022) e2206005, https://doi.org/10.1002/adma.202206005.

[52] K. Szlachetko, P. Piotrowski, K. Sadecka, P. Osewski, D. Kasprowicz, D.A. Pawlak, Selective surface-enhanced Raman scattering in a bulk nanoplasmonic Bi_2O_3-Ag eutectic composite, Nanophotonics *9* (2020) 4307–4314, https://doi.org/10.1515/nanoph-2020-0281.

[53] K. Sadecka, M. Gajc, K. Orlinski, H.B. Surma, A. Klos, I. Jozwik-Biala, K. Sobczak, P. Dluzewski, J. Toudert, D.A. Pawlak, When eutectics meet plasmonics: nanoplasmonic, volumetric, self-organized, silver-based eutectic, Adv. Opt. Mater. *3* (2015) 381–389, https://doi.org/10.1002/adom.201400425.

[54] K. Sadecka, J. Toudert, H.B. Surma, D.A. Pawlak, Temperature and atmosphere tunability of the nanoplasmonic resonance of a volumetric eutectic-based Bi_2O_3-Ag metamaterial, Opt. Express *23* (2015) 19098–19111, https://doi.org/10.1364/OE.23.019098.

[55] M. Ezawa, Antiferromagnetic topological superconductor and electrically controllable Majorana fermions, Phys. Rev. Lett. *114* (2015) 056403, https://doi.org/10.1103/PhysRevLett.114.056403.

[56] S.V. Eremeev, V.N. Men'shov, V.V. Tugushev, P.M. Echenique, E.V. Chulkov, Magnetic proximity effect at the three-dimensional topological insulator/magnetic insulator interface, Phys. Rev. B *88* (2013), https://doi.org/10.1103/PhysRevB.88.144430.

[57] K.-H. Jin, S.-H. Jhi, Proximity-induced giant spin-orbit interaction in epitaxial graphene on a topological insulator, Phys. Rev. B *87* (2013) 075442, https://doi.org/10.1103/PhysRevB.87.075442.

[58] L. Braun, G. Mussler, A. Hruban, M. Konczykowski, T. Schumann, M. Wolf, M. Munzenberg, L. Perfetti, T. Kampfrath, Ultrafast photocurrents at the surface of the three-dimensional topological insulator Bi_2Se_3, Nat. Commun. *7* (2016) 13259, https://doi.org/10.1038/ncomms13259.

[59] O.V. Misochko, J. Flock, T. Dekorsy, Polarization dependence of coherent phonon generation and detection in the three-dimensional topological insulatorBi_2Te_3, Phys. Rev. B *91* (2015), https://doi.org/10.1103/PhysRevB.91.174303.

[60] Jackson, K.A., and Hunt, J.D. (1988). Lamellar and Rod Eutectic Growth. In Dynamics of Curved Fronts, P. Pelcé, ed. (Academic Press), pp. 363-376. https://doi.org/10.1016/B978-0-08-092523-3.50040-X.

[61] D.A. Pawlak, K. Kolodziejak, K. Rozniatowski, R. Diduszko, M. Kaczkan, M. Malinowski, M. Piersa, J. Kisielewski, T. Lukasiewicz, $PrAlO_3$−$PrAl_{11}O_{18}$ eutectic: its microstructure and spectroscopic properties, Cryst. Growth Des. *8* (2008) 1243–1249, https://doi.org/10.1021/cg0609522.

[62] S. Nakajima, The crystal structure of $Bi_2Te_{3-x}Se_x$, J. Phys. Chem. Solids *24* (1963) 479–485, https://doi.org/10.1016/0022-3697(63)90207-5.

[63] C.I. Fornari, P.H.O. Rappl, S.L. Morelhão, E. Abramof, Structural properties of Bi_2Te_3 topological insulator thin films grown by molecular beam epitaxy on (111) BaF_2 substrates, J. Appl. Phys. *119* (2016) 165303, https://doi.org/10.1063/1.4947266.

[64] A. Dankert, J. Geurs, M.V. Kamalakar, S. Charpentier, S.P. Dash, Room temperature electrical detection of spin polarized currents in topological insulators, Nano Lett. *15* (2015) 7976–7981, https://doi.org/10.1021/acs.nanolett.5b03080.

[65] N.H. Tu, Y. Tanabe, Y. Satake, K.K. Huynh, K. Tanigaki, In-plane topological p-n junction in the three-dimensional topological insulator Bi2-xSbxTe3-ySey, Nat. Commun. *7* (2016) 13763, https://doi.org/10.1038/ncomms13763.

[66] R. Shikler, T. Meoded, N. Fried, B. Mishori, Y. Rosenwaks, Two-dimensional surface band structure of operating light emitting devices, J. Appl. Phys. *86* (1999) 107–113, https://doi.org/10.1063/1.370706.

[67] M.Z. Hasan, C.L. Kane, Colloquium: topological insulators, Rev. Mod. Phys. *82* (2010) 3045–3067, https://doi.org/10.1103/RevModPhys.82.3045.

[68] Y.L. Chen, J.H. Chu, J.G. Analytis, Z.K. Liu, K. Igarashi, H.H. Kuo, X.L. Qi, S.K. Mo, R.G. Moore, D.H. Lu, et al., Massive dirac fermion on the surface of a magnetically doped topological insulator, Science *329* (2010) 659, https://doi.org/10.1126/science.1189924.

[69] S. Akamatsu, S. Bottin-Rousseau, M. Şerefoğlu, G. Faivre, Lamellar eutectic growth with anisotropic interphase boundaries: experimental study using the rotating directional solidification method, Acta Mater. *60* (2012) 3206–3214, https://doi.org/10.1016/j.actamat.2012.02.033.

[70] A.A. Kulkarni, E. Hanson, R. Zhang, K. Thornton, P.V. Braun, Archimedean lattices emerge in template-directed eutectic solidification, Nature *577* (2020) 355–358, https://doi.org/10.1038/s41586-019-1893-9.

[71] D.A. Pawlak, K. Kolodziejak, S. Turczynski, J. Kisielewski, K. Rożniatowski, R. Diduszko, M. Kaczkan, M. Malinowski, Self-organized, rodlike, micrometer-scale microstructure of $Tb_3Sc_2Al_3O_{12}$–$TbScO_3$:Pr eutectic, Chem. Mater. *18* (2006) 2450–2457, https://doi.org/10.1021/cm060136h.

[72] J.W. Boley, K. Chaudhary, T.J. Ober, M. Khorasaninejad, W.T. Chen, E. Hanson, A. Kulkarni, J. Oh, J. Kim, L.K. Aagesen, et al., High-operating-temperature direct ink writing of mesoscale eutectic architectures, Adv. Mater. *29* (2017), https://doi.org/10.1002/adma.201604778.

[73] M.K. Abrikosov, V.F. Bankina, Study of the state diagram of Bi-Te, Zh. Neorg. Khim. *3* (1958) 659–667.

[74] S.H. Song, M.K. Joo, M. Neumann, H. Kim, Y.H. Lee, Probing defect dynamics in monolayer MoS_2 via noise nanospectroscopy, Nat. Commun. *8* (2017) 2121, https://doi.org/10.1038/s41467-017-02297-3.